2020-11-15

Reduced Arctic sea ice extent during the mid-Pliocene Warm Period concurrent with increased Atlantic-climate regime

Rahaman, W

10.1016/j.epsl.2020.116535
Earth and Planetary Science Letters
Elsevier BV

Reduced Arctic sea ice extent during the mid-Pliocene Warm Period concurrent with increased Atlantic-climate regime

*Waliur Rahaman[1], Lukas Smik[2], Deniz Köseoğlu[5], Lathika N[1], Mohd Tarique[1], Meloth Thamban[1], Alan Haywood[3], Simon T. Belt[2], J. Knies[4,5]

[1]National Centre for Polar and Ocean Research (NCPOR), Ministry of Earth Sciences, Vasco-da-Gama, Goa 403804, India

[2]School of Geography, Earth and Environmental Sciences, University of Plymouth, PL4 8AA, UK

[3]School of Earth and Environment, University of Leeds, Woodhouse Lane, Leeds, LS2 9JT, UK

[4]Geological Survey of Norway, N-7491 Trondheim, Norway

[5] CAGE – Centre for Arctic Gas Hydrate, Environment and Climate, Department of Geosciences, UiT The Arctic University of Norway, 9037 Tromsø, Norway

Revised submission to Earth and Planetary Science Letter (EPSL)

*Corresponding author (waliur@ncpor.res.in)

Orchid ID: https://orcid.org/0000-0001-6439-4529

Abstract

Quantifying the contribution of poleward oceanic heat transport to the Arctic Ocean is important for making future sea ice and climate predictions. To highlight its potential importance in a warmer world, we present a new record of water-mass exchange between the Atlantic and the Arctic Oceans using the authigenic neodymium isotopic composition of marine sediments from the Fram Strait during the past ~3.4 to 2.6 Ma. In this study, we target the mid-Pliocene Warm Period (mPWP: 3.264–3.025 Ma) of the Pliocene epoch, the most recent geological analogue for future climate change. We complement our semi-quantitative water mass exchange reconstruction with estimates of spring sea ice concentration based on source-specific biomarkers. Our estimates of volume transport of warm waters into the Arctic Ocean suggest long-term secular changes from the lowest during the Marine Isotope Stage M2 “glacial” (3.312–3.264 Ma), to near complete “Atlantification” of the Eurasian sector of the Arctic Ocean during the mPWP. Orbital forcing is found to be the dominant controlling factor for modulating northward volume transport of Atlantic-derived water masses, with an associated reduction in Arctic spring sea ice concentration of ~30-35%. Current generation models often produce diverging results, however, and have not yet been validated against proxy data in northern high latitude settings during the mPWP. Our new results of northward volume transport and sea ice extent therefore provide much needed input for validation of current generation models aimed at improving the robustness of future climate modelling in the Arctic.

Keywords: mid-Pliocene, North Atlantic Current, Arctic, Sea ice, Atlantification

1. Introduction

The most dramatic changes observed in the Arctic Ocean during the recent past are the unprecedented reductions in sea ice extent and thickness (Kinnard et al., 2011). Although coupled ice-ocean model simulations suggest that the recent warming in the Northern Hemisphere is responsible for this decline (Petrie et al., 2015), there is disagreement between data and models over the impact of atmospheric warming versus oceanic heat transport on sea ice decline (Ding et al., 2018; Dowsett et al., 2012; Haywood et al., 2013). Studies based on proxy reconstructions of heat and volume transport through the Fram Strait (Spielhagen et al., 2011), and in-situ observations in the eastern Arctic Ocean (Polyakov et al., 2017), suggest that enhanced oceanic heat transport by the North Atlantic Current (NAC) over the past few decades likely explains the weakened stratification, increased vertical mixing and reduced sea ice in the Atlantic sector of the Arctic, collectively termed “Atlantification” (Polyakov et al., 2017; Spielhagen et al., 2011). In order to improve our understanding about Arctic sea ice variability, particularly within the current context of rapid global warming, it is imperative to reconstruct sea ice conditions during previous warm climate states, and decipher the underlying mechanisms that control its distribution. One such period in Earth’s history is the Pliocene (5.33–2.58 Ma), which experienced higher global temperatures than pre-industrial (Dowsett et al., 2009), and was characterized by a gradual transition from relatively warm climates during the Early Pliocene towards cooler conditions in the Late Pliocene. Some previous organic geochemical-based proxy climate reconstructions for the Pliocene have been conducted for the North Atlantic and Fram Strait (Clotten et al., 2018; Knies et al., 2002), and similar studies have been carried out for other warm

interglacials such as the Eemian (Marine Isotope Stage (MIS) 5e) and the early Holocene (Belt et al., 2015; Müller et al., 2012; Stein et al., 2017). However, the roles of atmospheric warming versus northward heat transport in controlling sea ice conditions were not assessed as part of these studies.

Here we aimed to identify the potential impact of future changes in oceanic heat transport into the Arctic Ocean and the effects of “Atlantification” in a warmer than modern climate. To achieve this, we conducted a semi-quantitative assessment of northward volume transport of Atlantic water through the Fram Strait during a geological period when (1) climatic conditions in terms of temperature and atmospheric CO_2 level were analogous to modern/or future projected scenarios and (2) global oceanographic and tectonic settings were nearly identical to today. The mid-Pliocene Warm Period (mPWP: 3.264–3.025 Ma) is known to be warmer (globally) than today (Dowsett et al., 1992; Haywood et al., 2016), with atmospheric CO_2 concentrations estimated to be in the range 350-450 ppmv (Berends et al., 2019; Foster et al., 2017). Hence, the mPWP has been proposed as a possible reference for future warm climate states (IPCC, 2013). Confirmation of increased polar ocean heat transport and reduced sea ice in the Arctic Ocean during the mPWP (Raymo et al., 1996) would therefore be of clear benefit for the assessment of coupled ocean-ice-atmosphere model simulations of the mPWP (Haywood et al., 2016).

To achieve this objective, we first reconstructed an orbital-resolution record of watermass mixing between the NAC and Arctic-derived polar waters (PW) in the Fram Strait (Fig. 1), based on authigenic neodymium (Nd) isotopes (ε_{Nd}). The radiogenic isotope composition of Nd in seawater reveals changes in watermass mixing and

circulation patterns due to its quasi-conservative behavior (Martin, 2002) and lower average oceanic residence time (360–2000 years) compared to the global ocean mixing time ~1500 years (Tachikawa et al., 1999) . Critically, in contrast to stable oxygen ($\delta^{18}O$) or carbon isotope ($\delta^{13}C$) measurements, the Nd isotope ratios are not affected by isotopic fractionation resulting from any biological or other low-temperature processes, so represent a robust proxy for paleo-water mass circulation (Martin, 2002). In a modern context, the majority of Atlantic-derived water masses are transported northward into the Arctic Ocean along the Svalbard continental margin, which is the northernmost extension of the NAC (Fig. 1). This warm water submerges into the Arctic Ocean or is deflected westward and submerged southward below cold and less saline waters of the East Greenland Current (EGC). All of these modern water masses possess characteristic Nd isotope signatures (Fig. 1) (Laukert et al., 2017; Werner et al., 2014). Less radiogenic values are indicative of a stronger influence of NAC flowing into the Nordic Seas (present-day ε_{Nd} = -13.2 to -13.0) (Teschner et al., 2016) while more radiogenic Nd isotope signatures reflect enhanced contribution from Arctic-derived polar waters (PW) (Laukert et al., 2017) (e.g. ε_{Nd} = -9.9). For this study, an orbital-resolution (~5 ka) authigenic ε_{Nd} record was obtained through analysis of bulk sediments from Ocean Drilling Program (ODP) Hole 910C (hereafter referred to 910C) on the Yermak Plateau, eastern Fram Strait, (80°15.894'N, 6°35.430'E, water depth: 556.4 m) covering the interval between 3.4 Ma and 2.6 Ma. This new record is supplemented by a previously published low-resolution (60-70 ka) record of authigenic ε_{Nd} from ODP Hole 911A (80° 28.466′ N, 8° 13.640′ E, water depth: 902 m) (hereafter referred to 911A) at the eastern flank of the Yermak Plateau (Teschner et al., 2016).

To identify the corresponding changes in sea ice coverage and carbonate chemistry, the sea ice biomarker proxy IP_{25}, a related open-water highly branched isoprenoid (HBI) lipid (HBI III), and calcium carbonate ($CaCO_3$) abundance related to carbonate chemistry and productivity/or preservation, were also analyzed. Over the last decade, source-specific highly branched isoprenoid (HBI) lipid biomarkers have emerged as reliable proxies for reconstructing past sea ice extent in the polar oceans (Belt, 2018 and references therein). The most frequently studied biomarker is the mono-unsaturated HBI IP_{25}, first identified in Arctic sea ice and sediments by Belt et al. (2007), and has since been used as a binary measure of seasonal Arctic sea ice in the past for time scales ranging from recent decades to several millions of years. Further, by combining sedimentary IP_{25} concentrations with those of various phytoplankton biomarkers in the form of the IP_{25}-phytoplankton (PIP_{25}) index, semi-quantitative estimates of sea ice extent can be achieved (Belt, 2018; Müller et al., 2011). Finally, when a further tri-unsaturated HBI (often referred to as HBI III; Belt et al., 2015) is used as the open water counterpart to IP_{25}, the resulting PIP_{25} index (i.e. $P_{III}IP_{25}$) exhibits a reasonably good linear relationship to spring sea ice concentration (%SpSIC) for the Barents Sea and neighboring regions (Smik et al., 2016).

North Atlantic and Arctic waters are characterized by distinct carbonate characteristics (e.g. alkalinity and pH), so carbonate abundance in sediments from the Fram Strait (mixing zone) can be used to infer changes in carbonate chemistry, productivity, preservation and dissolution resulting from variable paleo-oceanographic changes. For example, warm and carbonate-rich North Atlantic waters lead to better preservation compared to cold carbonate depleted Arctic waters. However, one of the

caveats attached with the application is the input of detrital carbonate to the core site. Study of carbonates in the core sites ODP 909 (Fram Strait) and 911 (Yermak Plateau) have suggested that predominant fractions of the carbonate abundance in the sediments are of authigenic origin and therefore controlled carbonate abundance variability in the Fram-Strait (Chow et al., 1996). Further, in previous studies, therefore, high carbonate preservation in sediments from the Fram Strait has been attributed to increased influence of Atlantic water masses (Zamelczyk et al., 2014). In the Norwegian–Greenland Sea, high carbonate content has also been interpreted to reflect the influence of warm Atlantic water masses, while low carbonate content were attributed to cold surface waters (Huber et al., 2000). Therefore, a combined authigenic Nd isotope and carbonate record from the Fram-Strait were employed in the present study to reconstruct northward volume and heat transport by the NAC.

2. Material and methods

Sediments of ODP Hole 910C (80°15.894' N, 6°35.430' E; water depth: 556.4 m) have been analyzed in this study. The deep-water Nd isotope signal was extracted from the Fe-Mn oxyhydroxide fraction of bulk sediment following the leaching procedure described below. Further details of Nd isotopes, HBI biomarkers and calcium carbonate abundance measurements are given in the following sections.

2.1 Neodymium isotope analysis in authigenic fractions

We measured the neodymium (Nd) isotope composition in authigenic phases extracted from the bulk sediments of 910C. This new record of authigenic ε_{Nd} is supplemented by an earlier published low-resolution (60-70 ka) record from ODP Hole 911A at the

eastern flank of the Yermak Plateau (Teschner et al., 2016). Therefore, for comparison, and to avoid discrepancies related to the analytical methods for the extraction of authigenic Nd from sediments and its isotope measurements, we adopted the same method of Teschner et al. (2016). The procedure thus began with extracting the past seawater signal contained in the diagenetic coatings from ~2 g of sample material with a 0.05 M hydroxylamine hydrochloride and 15% acetic acid solution (HH leach), buffered to a pH of ~3.5 to 4.0, without rinsing before the HH leach. The rare earth elements (REEs) in the solution were separated using cation exchange columns filled with AG50WX8 resin (mesh 200–400). Nd was separated from the other REEs using columns filled with Ln-Spec resin (50–100 mesh). Nd isotopes were analyzed using a multi-collector inductively coupled plasma mass spectrometer (MC-ICP-MS, Thermo Scientific Neptune Plus) at the National Centre for Polar & Ocean Research (NCPOR), Goa, India. All Nd isotope ratios ($^{143}Nd/^{144}Nd$) presented here were corrected for mass bias following an exponential law using the known value of $^{146}Nd/^{144}Nd$ of 0.7219. The instrument bias was normalized to the accepted $^{143}Nd/^{144}Nd$ value of the JNdi-1 standard of 0.512115 (Tanaka et al., 2000). Repeat measurements of the JNdi-1 standard yielded a long-term average reproducibility of ±0.3 ε_{Nd} (2σ; n = 103) over a period of nine months. Average procedural blank ascertained for Nd (n = 4) was 170 pg which is less than 1% of the total Nd analyzed in samples, so blank correction was not applied. All Nd isotope ratios are reported in epsilon notation according to Equation 1.

$$\varepsilon_{Nd} = \left[\frac{^{143}Nd/^{144}Nd_{sample}}{^{143}Nd/^{144}Nd_{CHUR}} - 1\right] \times 10^4 \qquad Eq\ (1)$$

In order to check the quality of the authigenic Nd isotope analyses, which includes chemical extractions of the authigenic Nd and its isotopic measurements, we analyzed a

total of 16 replicates. Data from these replicates (with a variable range of ε_{Nd}) are highly consistent (Supplementary Fig. S1); most of them are falling on the equiline (1:1 line).

2.2 HBI biomarkers

The HBI biomarkers IP_{25} and HBI III were extracted from freeze-dried subsamples (~2–4 g) from 910C. Samples were saponified in a methanolic KOH solution (~5 mL H_2O: MeOH (1:9); 5% KOH) for 60 min (70 °C). Hexane (3×2 mL) was added to the saponified content, with supernatant solutions, containing non-saponifiable lipids (NSLs), transferred with glass pipettes to clean vials and dried over a gentle stream of N_2 to remove traces of H_2O/MeOH. NSLs were then re-suspended in hexane (0.5 mL) and fractionated using column chromatography (SiO_2; 0.5 g). Non-polar lipids, including IP_{25} and HBI III, were eluted with hexane (6 mL). Each non-polar fraction was further purified to remove saturated components using silver-ion chromatography (Belt et al., 2015) with saturated compounds eluted with hexane (2 mL) and unsaturated compounds, including HBIs, collected in a subsequent acetone fraction (3 mL). Prior to extraction, samples were spiked with an internal standard (9-octylheptadec-8-ene, 9-OHD, 10 μL; 10 μg mL^{-1}) to permit quantification of HBIs. Analysis of fractions containing IP_{25} and HBI III was carried out using gas chromatography–mass spectrometry (GC–MS) following the methods and operating conditions described elsewhere (Belt et al., 2012). Mass spectrometric analysis was carried out in total ion current (TIC) and selected ion monitoring (SIM) modes. The identification of IP_{25} and other HBIs was based on their characteristic GC retention indices (e.g. RI_{HP5MS} = 2081 and 2044 for IP_{25} and HBI III, respectively) and mass spectra (Belt, 2018). Quantification of all HBIs was achieved by comparison of mass spectral responses of

selected ions (e.g. IP_{25}, *m/z* 350; HBI III, *m/z* 346) in SIM mode with those of the internal standard (9-OHD, *m/z* 350) and normalized according to their respective instrumental response factors, derived from solutions of known biomarker concentration, and sediment masses (Belt et al., 2012).

Concentrations of IP_{25} and HBI III were combined in the form of the $P_{III}IP_{25}$ index (Eq. 4), with the latter then used to provide semi-quantitative estimates of spring sea ice concentration (SpSIC (%), Eq. 5) according to a recent regional calibration (Smik et al., 2016). A root mean-square error of 11% associated with SpSIC estimates, was also calculated using regional calibration data (Köseoğlu et al., 2018; Smik et al., 2016)

$$P_{III}P_{25} = \frac{IP_{25}}{(IP_{25} + (0.63 * HBI\ III)} \qquad Eq\ (4)$$

$$SpSIC\ (\%) = \frac{(P_{III}IP_{25} - 0.0692)}{0.0107} \qquad Eq\ (5)$$

Finally, we used the non-parametric CP3O algorithm from the R package ECP (R Core Team, 2018) to carry out change-point analysis on SpSIC estimates to identify significant shifts in the time series profile (Supplementary Fig. S2). All biomarker and %SpSIC data are provided in Supplementary Data 2.

2.3 Analysis of carbon

Analyses of total carbon (TC) and organic carbon (C_{org}) were performed with a LECO SC-632 at the Geological Survey of Norway, Trondheim. For TC determination, subsamples of 300-400 mg were combusted at 1350°C and the release of CO_2 was measured. For C_{org} analysis, sub-samples of 400-450 mg were placed in carbon-free pervious ceramic combustion boats. These were placed on a heating plate at 50°C (± 5°C) and treated with 10 vol.% hydrochloric acid (HCl) to remove inorganic carbon

(carbonate) and subsequently rinsed with distilled water and dried in the drying oven prior to analysis. Carbonate content was calculated as $CaCO_3$ = (TC- C_{org}) x 8.33 with an assumption that calcite is the dominant form in the carbonate fraction (Vogt et al., 2001). Results are provided in weight percentage (wt. %) and the standard deviation of the TC and C_{org} measurements based on the repeated measurements of a standard was ± 0.026 wt% (1σ, n=8) and ± 0.028 wt. % (1σ, n=11), respectively.

2.4 Age control for sediments deposited at ODP Hole 910C

The age constraints for 910C is based on correlation of bio-stratigraphic and magneto-stratigraphic datums with Hole 911A together with additional benthic stable isotope data from 910C for the Pliocene (2.44 – 5.76 Ma). The age model based on the tie points and associated uncertainties have already been discussed in previous studies (Grøsfjeld et al., 2014; Knies et al., 2014b; Mattingsdal et al., 2014). Briefly, five tie points formed the basis of the age model for our target interval between ~3.4 and 2.6 Ma in 910C (see Supplementary Table S1). Two tie-points at 190 mbsf and 305 mbsf inferred from seismic correlation between 910C and 911A mark the magneto-stratigraphic boundaries at 2.58 Ma (Matuyama/Gauss) and 3.6 Ma (Gauss/Gilbert) (Mattingsdal et al., 2014). Support for this age model is provided by the biostratigraphic “Datum A” (~2.78 Ma) at ~223 mbsf in 910C (Sato and Kameo, 1996) and the glacial to interglacial oscillations of the benthic $\delta^{18}O$ record of 910C (Knies et al., 2014a). Between “Datum A” (2.78 Ma) and the inferred Gauss/Gilbert boundary (3.6 Ma), we have originally applied an age model based on linear sedimentation rates between these two fix-points (Knies et al., 2014a). One major climate transition (i.e. MIS M2 glaciation) expressed by a sharp increase in the global $\delta^{18}O$ stack (Lisiecki and Raymo,

2005) (Supplementary Fig. S4) falls within our targeted time interval of 3.4 to 2.6 Ma. We used the more radiogenic ε_{Nd} peak at 260.4 mbsf in 910C as an additional tie point to define the MIS M2 glaciation (Supplementary Table S1, Supplementary Fig. S5), corresponding to a pronounced IRD pulse in Hole 911A (Supplementary Fig. S6). The calculated sedimentation rates between fix points either side of this new tie point are within the same order of magnitude (8 to 15 cm/ka) thus justifying this additional age fix point. The age of the “Datum A” corresponding to the depth 223 mbsf was constrained based on the occurrence of calcareous nanofossils in 910C and 911A (Sato and Kameo, 1996) and is slightly shifted from the original age of 2.78 Ma (Knies et al., 2014b) to 2.83 Ma in the revised age model (Supplementary Table S1). Together with the new tie points for biostratigraphic “Datum A” and shifted radiogenic ε_{Nd} peak to MIS M2, we used the linear sedimentation rates between all tie points to establish the age model for 910C between 3.4 - 2.6 Ma (Supplementary Table S1). Based on the revised chronology, the most negative excursion in the authigenic ε_{Nd} profile is now shifted from 2.981 to 3.081 Ma, while the most positive excursion defines the MIS M2 glaciation (Supplementary Fig. S4). Considering the uncertainty in our age model, it might be challenging to resolve all individual peaks and troughs corresponding to glacial-interglacial stages in our proxy records of authigenic ε_{Nd}, biomarkers and $CaCO_3$; however, the most prominent excursions in our proxy records during the mPWP can be resolved with confidence, which is the primary target interval of the present study. All information on previously published and new tie points are provided in Supplementary Table S1.

3. Results

3.1 Authigenic ε_{Nd} record from the Yermak Plateau.

The new ε_{Nd} record from the Yermak Plateau allows identification of the maximum limit of water mass exchange between the NAC and Arctic derived PW, particularly during the major climatic transitions of the Pliocene to the earliest Pleistocene (3.4–2.6 Ma). These include the MIS M2 glaciation (3.312–3.264 Ma), the mPWP (3.264–3.025 Ma) and the intensification of Northern Hemispheric glaciation (iNHG) at ~2.7 Ma ago. The authigenic ε_{Nd} record shows long-term secular changes from -9.2 during the MIS M2 glacial period to -14.4 (5.2 ε_{Nd} unit) during the mPWP; the modern value of -11.7 reported (Lambelet et al., 2016) from the core site falling within this range. Thereafter, an increasing trend up to -7.8 at ~2.6 Ma is clearly discernable, with several prominent positive excursions associated with iNHG cold stages (Fig. 2c). Our ε_{Nd} record for 910C exhibits a larger range (6.6 ε_{Nd} unit) compared to that of 911A (3.4 ε_{Nd} unit) (Teschner et al., 2016) within the time period 3.5 – 2.5 Ma (Fig. 2c), most likely due to the higher temporal resolution.

3.2 Biomarker and $CaCO_3$ records.

The occurrence of seasonal sea ice throughout the record is confirmed by the near continuous presence of the biomarkers IP_{25} and HBI III (Fig. 2d). Although the concentration of HBI III is mainly lower than that of IP_{25}, it is the more abundant biomarker during the mPWP (ca. 3.150–2.970 Ma), consistent with more productive open-water conditions, as also shown by the carbonate record, which reaches its highest values during the MIS KM1-K2 (~3.150-3.050 Ma) (Fig. 2f). The $CaCO_3$ abundance measured in the bulk sediments ranges from 0.5 to 6%; however, a sharp

three fold increase from the mean value ~2% to 6% is evident during the mPWP, which coincides with the prominent negative excursion in the ε_{Nd} record (Fig. 2c).

4. Discussion

The authigenic ferromanganese oxyhydroxide fraction extracted from the bulk sediments has been demonstrated to record the ε_{Nd} signal of bottom waters of the Yermak Plateau (Teschner et al., 2016; Werner et al., 2014). Hence, temporal variations in authigenic ε_{Nd} during glacial-interglacial periods have been primarily attributed to watermass exchange between the NAC and PW, changes in sediment provenance, and variable weathering input due to glacial erosion (Teschner et al., 2016). However, other factors/mechanisms that contributed to the past authigenic ε_{Nd} variability are discussed in the following section.

4.1 Factors contributing to past authigenic ε_{Nd} variability

ODP Hole 910C is placed in the mixing zone between Atlantic- and Arctic-derived waters (Fig. 1) and is therefore well suited to monitor the relative influence of two water masses: (i) relatively warmer, high salinity water (i.e. the NAC characterized by a less radiogenic Nd isotope signature and (ii) relatively cold and less saline water (i.e. Arctic-derived PW) characterized by more radiogenic Nd isotopes. In the open ocean away from ocean margins and regions of deep-water formation, Nd appears to behave quasi-conservatively (Rempfer et al., 2011). Therefore, the variability in authigenic ε_{Nd} record from the open ocean is mainly explained by the mixing of water masses with distinct ε_{Nd} signatures (Lang et al., 2016). However, contributions from other sources of dissolved Nd can substantially influence the authigenic ε_{Nd} record.

Assuming that the modern geological and tectonic setting of the study region have largely remained stable over the past ~4.6 Ma (Knies et al., 2014a), we discuss the following potential mechanisms and factors that may have contributed to the variability and changes in the authigenic ε_{Nd} record of 910C: (i) changes in weathering regimes and sediment sources; (ii) boundary exchange processes; and (iii) volumetric exchange of the NAC and PW.

Dissolved radiogenic isotope signatures in seawater originate from weathering processes of the continental crust (Frank, 2002) and, therefore, the glacial-interglacial changes in chemical weathering could influence the ε_{Nd} record. Teschner et al. (2016) reconstructed past water mass mixing and erosional inputs prior and post intensification of Northern Hemisphere glaciation (iNHG, ~2.7 million years ago) based on records of radiogenic isotopes of Sr, Nd and Pb at ODP Hole 911A. Changes in the authigenic ε_{Nd} record were highlighted for two different scenarios; (i) prior to the iNHG, the Pb and Nd isotopes composition was characterized by unradiogenic values and low variability due to the limited extent of ice sheets. These observations are consistent with earlier inferences from the Arctic Ocean (Haley et al., 2007) and suggest constant erosional supply of material to the Yermak Plateau, most likely from local sources (i.e. Svalbard). (ii) After the iNHG, conditions changed dramatically with higher-amplitude ε_{Nd} variability in both deep waters and detrital sediments inputs due to changes in weathering inputs associated with the waxing and waning of the Eurasian ice sheets, water mass exchange and increased supply of ice-rafted debris (IRD). Comparison of the IRD record (Knies et al., 2014b) with our ε_{Nd} record, shows higher IRD flux during the periods of MIS M2 glaciation and iNHG (~2.7 Ma), and low and stable IRD fluxes during

the mPWP (Supplementary Fig. S6). The latter corresponds to the IRD record from Site U1307 on Eirik Drift where coarse IRD is largely absent during the mPWP, and IRD is only present in small abundances during (de)glacials between ~3 Ma and 2.75 Ma. Therefore, higher variability in IRD supply and change of its sources could influence the authigenic ε_{Nd} record in 910C; however, this can be excluded for the interglacial periods prior to the iNHG, particularly during the mPWP. It is also important to note that the timing of the iNHGs was further shifted to post MIS G2 (2.64 Ma) based on the Pb isotope and geochemical studies of the IRD on the lower eastern flank of the Reykjanes Ridge (Bailey et al., 2013). Therefore, we suggest that the observed variability and changes in the radiogenic Nd isotope record in 910C is affected by glacial weathering input probably during the MIS M2 glaciation and after the iNHG. In contrast, it is unlikely to be significantly affected by the changes in chemical weathering inputs and/sediment transport from distant sources during our targeted time interval of mPWP due to the stability of the climatic conditions and glacial erosion was rather limited.

The chemical weathering of Iceland-derived basaltic material can influence the Nd isotope composition of the NAC resulting in a shift towards more radiogenic values. However, in an earlier study, it has been suggested that present day exchange with Iceland derived basaltic material does not affect the deep water ε_{Nd} signature of the main path of North Atlantic inflow, although it can influence the signature of southward flowing currents such as the East Greenland Current (Chen et al., 2012; Lacan and Jeandel, 2004).

Seawater interactions with the continental margins (boundary exchange) could be a potential source for radiogenic isotope signatures of seawater, particularly in the

Nordic Seas where basaltic formations are highly susceptible to dissolution and exchange with seawater (Chen et al., 2012; Lacan and Jeandel, 2004). The effects of boundary exchange have been reported from different continental margins in the subpolar regions including the Nordic Seas, and model results confirmed the importance of this input mechanism (Rempfer et al., 2011). Due to the large shelf areas of the Arctic Ocean, boundary exchange might be expected to be significant, although the water column data available so far do not provide clear evidence for this process (Andersson et al., 2008). Further, Laupkert et al (2017) suggested recently that ε_{Nd} values around -10 are present in the eastern and western Fram Strait below ~500 m, implying that there is no evidence for boundary exchange processes influencing the ε_{Nd} record to a significant extent on the Yermak Plateau.

In summary, with the absence of any significant ice-rafting prior to ~2.7 Ma (except MIS M2) in the Nordic Seas (Fig. 2e), increased sea surface temperatures (SST) by 3–7°C (Lawrence et al., 2009) between 3.4 and 2.6 Ma compared to the Holocene mean annual SST (Fig. 2g; dashed line) (Calvo et al., 2002), and thus no widespread Northern Hemisphere glacial advances, we attribute the large range in ε_{Nd} (-14.8 to -9.0) in 910C prior to the iNHG to changes in watermass circulation rather than to variable glacial weathering input. As such, the prominent negative excursion in the ε_{Nd} record during the mPWP (i.e. -14.4 ε_{Nd} units; Fig. 2c) is most likely due to an increase in volume transport of the NAC, resulting in an Atlantic-dominated climate regime of the Eurasian sector of the Arctic Ocean. Further, the prominent negative excursion in ε_{Nd} record coincides with a sharp three-fold increase in $CaCO_3$ abundance during the mPWP (Fig. 2f). This suggests an increased flow of warm NAC with higher

pH resulted in better preservation of carbonate and/or increase in productivity during interglacial periods in the eastern Fram Strait (Supplementary Figs. S7b, d, e), consistent with earlier reports from modern and Quaternary sediments (Huber et al., 2000).

To test the hypothesis of increased “Atlantification” and its concurrent sea ice decline further, we quantified the volumetric changes of the AW-derived water masses and sea ice concentration at 910C using (1) a simplified binary mixing model by constraining the end member values of ε_{Nd} for two water masses and (2) semi-quantitative estimates of spring sea ice concentration (%SpSIC) based on a regional calibration of biomarker distributions in modern sediments (Smik et al., 2016).

4.2 Quantifying water mass exchange based on authigenic ε_{Nd} record

Compilation and reassessment of seawater Nd data from the literature shows that the characteristic NAC ε_{Nd} signature near its origin in the inter-gyre region (north of 46° N) displays ε_{Nd} values between -14.0 ± 0.3 and -15.1 ± 0.3 (Dubois-Dauphin et al., 2017), which changes gradually during transport across the Arctic Mediterranean due to mixing of more radiogenic signatures of PW (ε_{Nd} = -9.9 ± 0.7, 1 SD (standard deviation) and [Nd] =27.1) (Laukert et al., 2017). We have assigned ε_{Nd} and [Nd] values for the NAC (-15 ± 1 (1 SD) and 16 ± 1 pmol/kg) and PW (-9.9 ± 1 (1 SD) and 27± 1pmol/kg) end-members, respectively, which are clearly distinct from the modern value in the Fram Strait (mean ε_{Nd} = -11.7 ± 0.8 (2SD)) (Laukert et al., 2017). With this identification of suitable end-member values for ε_{Nd}, we therefore adopt a simple binary mixing approach for the determination of the percentage Atlantic water component (%AWC) on the assumption that Nd behaves quasi-conservatively and end-member compositions

were invariant during the studied time interval. Such assumptions are discussed in more detail in the Supplementary Note 2. Meanwhile, we note that this method was successfully employed in a previous study (Lang et al., 2016) using a Nd isotope record from the late Pliocene (3.3–2.4 Ma ago) to quantify the mixing proportion of southern source water and north Atlantic deep water (NADW) in the North Atlantic.

4.2.1 Binary estimates of Atlantic water mass mixing using authigenic ε_{Nd} record

We have used the ε_{Nd} record from 910C to generate the semi-quantitative estimate of water-mass mixing between NAC and PW during the Late Pliocene to early Pleistocene (~3.4 - 2.6 Ma). The underlying assumptions of this approach are: (i) Nd isotopes exhibit quasi-conservative behaviour, (ii) mixing of Atlantic- and Arctic-derived waters at 910C is binary, and (iii) modern day end-members have been invariant between 3.4 and 2.6 Ma. We used the following binary mixing equation constrained by our current understanding of end-member compositions:

$$\varepsilon_{Nd_{910C}} = \frac{\varepsilon_{Nd_{AW}} * C_{AW} * f_{AW} + \varepsilon_{Nd_P} * C_{PW} * f_{PW}}{C_{AW} * f_{AW} + C_{PW} * f_{PW}} \qquad Eq\ (2)$$

$$f_{AW} + f_{PW} = 1 \qquad Eq\ (3)$$

where $\%AWC_{\varepsilon_{Nd}} = f_{AW} * 100$ is the relative contribution of Atlantic water component to 910C ($\%PWC_{\varepsilon_{Nd}}$ = 100 - $\%AWC_{\varepsilon_{Nd}}$), C_{PW} and C_{AW} represent the concentration of Nd in the Arctic (PW) and the Atlantic (AW), ε_{Nd910C} is the value of Nd isotope compositions of sediment leach from 910C, and ε_{AW} and ε_{PW} are the end-members of isotope composition of Atlantic and Arctic water masses, respectively. f_{AW} and f_{PW} represent the fractions of Nd coming from the Atlantic (AW) and Arctic (PW) waters.

In order to validate the use of this binary mixing model to 910C, we also calibrated our approach by comparison of semi-quantitative estimates of modern day volume transport with in situ observations. We thus estimated the modern day volume transport of NAC using a contemporary ε_{Nd} value at the borehole site of 910C and compared that with a mooring-based observation (Beszczynska-Moeller et al., 2012). Our estimate of %NAC based on ε_{Nd} (47 ± 9%) (Supplementary Fig. S9) compares well with a value of 45 ± 5% (Supplementary Fig. S9b) measured from an array of moorings in Fram Strait (78° 50′ N) over the period 1997–2010 (Beszczynska-Moeller et al., 2012).

We have determined the uncertainty associated fractions of NAC volume estimates using a Monte-Carlo error propagation method with 10,000 iterations in MATLAB, which is represented as an error envelop (at 95% confidence) (Fig. 3a). However, we offer some caution that our %NAC estimates may be subject to changes in the future when more suitable archives allow generation of orbital resolution records of NAC and PW end-member behaviour. For now, the uncertainties reported here for our ε_{Nd}-based estimates of %NAC may be underestimated due to limited knowledge of end-member ε_{Nd} values for Atlantic and Arctic waters. On the other hand, our main conclusions over our targeted time interval (3.4 – 2.6 Ma) are not influenced by such uncertainties.

Our estimates of %AWC in 910C indicate three distinct peaks with values close to 100%, indicating the presence of a dominant Atlantic watermass in the water column during the three interglacial events (Haywood et al., 2013) (i.e. MIS KM3, K1, and G17) within or close to the mPWP; albeit within the limitation of the age constraints of 910C

(Fig. 3 a). For MIS KM5c, with near-modern orbital configuration, the %AWC (51 ± 11%) was similar to today (45 ± 5%) (Beszczynska-Moeller et al., 2012; Zhang et al., 2013) but was close to ~0% during the preceding MIS M2 glaciation (3.305–3.285 Ma) (Fig. 3a), consistent with previous observations of a weaker NAC and concurrent cooling in the circum-Arctic (De Schepper et al., 2015). Importantly, although %AWC estimates for the glacial periods (i.e. MIS M2 and iNHGs) might potentially suffer higher uncertainty due to enhanced IRD flux and weathering inputs associated with higher glacial activity, such effects during the mPWP are likely insignificant, in practice, due to the relatively stable climate and lower IRD fluxes (Blake-Mizen et al., 2019; Knies et al., 2014a) (Fig. 2e and Supplementary Fig. S6). Pertinent to our reconstructed reduced flux of %AWC during the MIS M2 glaciation, we note that a similar situation has been reported for MIS6 based on authigenic coupled isotope records of Nd and Hf from the central Arctic Ocean (Chen et al., 2012).

4.2 Sea ice reconstruction

Extensive sea ice cover (>60% SpSIC) prevailed from 3.36–3.18 Ma, including maximum extent during MIS M2 (Fig. 3b). Thereafter, %SpSIC reduced substantially. According to Smik et al. (2016), biomarker-based %SpSIC estimates above ca. 68% also imply the occurrence of some summer sea ice ((>5% summer sea ice concentration (SuSIC)) (Supplementary Fig. S3). Similarly, while the occurrence of some summer sea ice was a common feature up to ca. 3.18 Ma (Fig. 3b), coincident with consistently low %AWC (i.e. below the modern value of 45%; Fig. 3a), ice-free summers were likely a common feature at the Yermak Plateau thereafter, especially during the mPWP. Change-point analysis carried out on our %SpSIC estimates shows

a statistically significant decrease of ca. 30–35% starting at ca. 3.15 Ma before increasing again at ca. 2.97 Ma (Supplementary Fig. S2). Prior to this, extensive sea ice cover similar to the modern (spring) maximum prevailed, including maximum extent during MIS M2 when the %AWC was at a minimum (Fig. 3a, b). The reduction in SpSIC during the mPWP likely reflects a response to increased %AWC, analogous to observations made for eastern Fram Strait (Spielhagen et al., 2011) and the Barents Sea spanning recent decades/centuries (Cabedo-Sanz and Belt, 2016). Similar observations have been reported for the Early Holocene and the Last Interglacial (MIS5e/Eemian), implying that increased Atlantic Water inflow is one important factor controlling sea ice conditions in an area covering northern Svalbard/Yermak Plateau and the northern Barents Sea continental margin (Belt et al., 2015; Müller et al., 2012; Stein et al., 2017). According to our SpSIC estimates, maximum sea ice extent during the mPWP exhibited a closer resemblance to that of modern-day late summer (i.e. minimum) conditions (Fig. 3b). These new data support the boundary conditions used in the Pliocene Research, Interpretation and Synoptic Mapping (PRISM) project, which assumes a conservative sea ice extent, an ice-free Arctic Ocean in summer, and winter sea ice conditions approximately equivalent to modern summer ice extent (Dowsett et al., 2010).

4.3 Forcing factors modulating North Atlantic volume transport and its impact

Our new reconstructions of watermass mixing and carbonate abundances follow the periodicities of eccentricity (~100 ka), obliquity (~40) and precessional cycles (~20 ka) (Figs. 4a, b). Further, the %AWC and %SpSIC records show good alignment with the eccentricity (Fig. 4c) and summer insolation in the northern hemisphere (Fig. 5b),

implying orbitally-paced control over changes to oceanic heat flow into the Arctic Ocean. Cross wavelet analysis highlights the common highest power between these two time series in colour bands (Fig. 4c). The vector arrows indicate an in-phase relation (pointing rightward) during 3.2 – 2.9 Ma at the eccentricity band (64 – 128 ka), implying that orbitally-controlled, enhanced NAC contribution resulted in an increase in marine productivity and reduction in sea ice coverage during the mPWP (Supplementary Fig. S7c, d). In particular, during the three interglacials with high eccentricity (i.e. KM3, K1, and G17; Fig. 5a, d), increased seasonality combined with warmer summers (higher solar insolation) in the Northern Hemisphere (Fig. 5a, b) may have resulted in an increased oceanic heat transport with consequential decline in Arctic sea ice extent and polar amplification of this warming. Alternatively, an orbitally-forced reduction in Arctic sea ice coverage may have changed buoyancy and salinity in the Atlantic, and thus been responsible for increased northward ocean heat transport during mPWP interglacials leading to a strongly positive ice-albedo feedback. Our proxy data do not reveal any correspondence with variable atmospheric CO_2 estimates (Fig. 5c, d and e) implying only a minor influence of greenhouse gas-derived radiative forcing in modulating NAC heat transport and reduction in Arctic sea ice. Further, tectonic changes could have driven circulation changes as has been reported for the Bering Strait and Nordic Sea related to reconfiguration of oceanic gateways (De Schepper et al., 2015; Horikawa et al., 2015). However, the strong signal of orbital cycles in our proxy records clearly indicate that the orbital forcing played the dominant role over all other controlling factors.

Based on multi-proxy records, it has been inferred that the Atlantic Meridional Overturning Circulation (AMOC) was significantly stronger in the mPWP compared to today (Raymo et al., 1996; Frank et al., 2002; Dowsett et al., 2009), which could have contributed to enhanced northward heat transport during the mPWP interglacials (Dowsett et al., 2009; Lawrence et al., 2010; Naafs et al., 2012), consistent with our findings. However, the exact mechanism(s) responsible for changes in northward heat transport remain a topic of debate (Haywood et al., 2016; Haywood et al., 2013; Zhang et al., 2013), but could potentially be resolved through further ocean modelling studies that integrate the new proxy data presented herein.

Regardless of the ultimate driver(s), our estimates of %AWC show a clear dominance of a warm and well-mixed Atlantic-dominated climate regime in the Eurasian Arctic during MIS KM3, K1, and (within the given age uncertainties) G17, with lower than modern sea ice extent (including ice-free summers) and higher marine productivity, consistent with modeled and reconstructed amplification of Arctic surface temperatures (Ballantyne et al., 2013), and a rise in annual mean surface air temperatures between 4°C to 5°C (Δt= Plio-KM5c – pre-industrial) (Prescott et al., 2018). This implies that the increase in %AWC with concurrent reduction in %SpSIC during these mPWP interglacials resembles modern observations of an advanced “Atlantification” of the study region (Cabedo-Sanz and Belt, 2016; Naafs et al., 2010; Spielhagen et al., 2011).

The conclusion of increased “Atlantification” of the Arctic during the mPWP from our new proxy records from the Atlantic-Arctic gateway confirms previous studies from lower latitudes a (Naafs et al., 2010; Raymo et al., 1996). Since current generation models have not yet been validated against any proxy-based observations of

“Atlantification” in the Eurasian sector of the Arctic during the mPWP, our new Nd isotope, biomarker and $CaCO_3$ records thus provide important input for testing the robustness of future climate modelling for northern high latitude settings.

5. Conclusions

Our new Nd isotope record of past water mass exchange in the Atlantic-Arctic gateway relative to the modern-day setting suggests a near doubling of NAC volume transport during mPWP interglacials KM3, K1, and G17 with different orbital configurations and thus stronger seasonality than today. This resulted in a warm and well-mixed Atlantic-dominated climate regime (“Atlantification”) of the Eurasian sector of the Arctic Ocean, reduced spring sea ice concentration, and the possibility of ice-free conditions during summers. In contrast, the mPWP interglacial with near-modern orbits (MIS KM5c) does not show significant deviation from today’s NAC volume transport or sea ice extent. This study demonstrates a dominant role of orbital forcing in modulating northward ocean heat transport and Arctic sea ice coverage during the mPWP. It also highlights the importance of improving data-model comparison studies for the Arctic Ocean that integrate reconstructions of water mass flow and ocean circulation, as well as temperature and sea ice, for climate states of the past that may be analogous to the future.

Data availability

All the data are provided in the supplementary and also will be archived in PANGEA upon acceptance of the manuscript.

Code availability

The MATLAB codes for uncertainty estimates on the volumetric water fractions of Atlantic water are available from the corresponding author W. Rahaman on request.

Acknowledgements

We acknowledge Ministry of Earth Sciences, Govt. of India, NCPOR, and Research Council of Norway through its funding scheme for CAGE (223259) and PACT (248793). We thank Manish Tiwari for his support as a Co-PI in the PACT project. We thank C Torrence, GP Compo, A Grinsted, JC Moore, and S Jevrejeva for MATLAB codes. Authors thank Priya Lokhande for initial handling of the sample for Nd isotope chemistry and Rohit Srivastava for providing MATLAB codes for Monte-Carlo error propagation. We thank two anonymous reviewers who provided supportive and constructive feedback on the initial version of this manuscript. Finally, we thank Laura F Robinson for editorial handling of the manuscript.

Author contributions

W.R., J.K. and M.T. designed the study. W.R., J.K., S.T.B and A.H wrote most of the text. Analysis of model results was completed by A.H and J.T. Mo.T. and L.N. analyzed authigenic Nd isotope compositions in bulk sediment. L.S, D.K and S.T.B. measured the concentrations of the IP_{25} and HBI III biomarkers in bulk sediments and interpreted outcomes. All authors contributed to interpreting results, discussion and improvement of this paper.

Competing interests

The authors declare no competing interests.

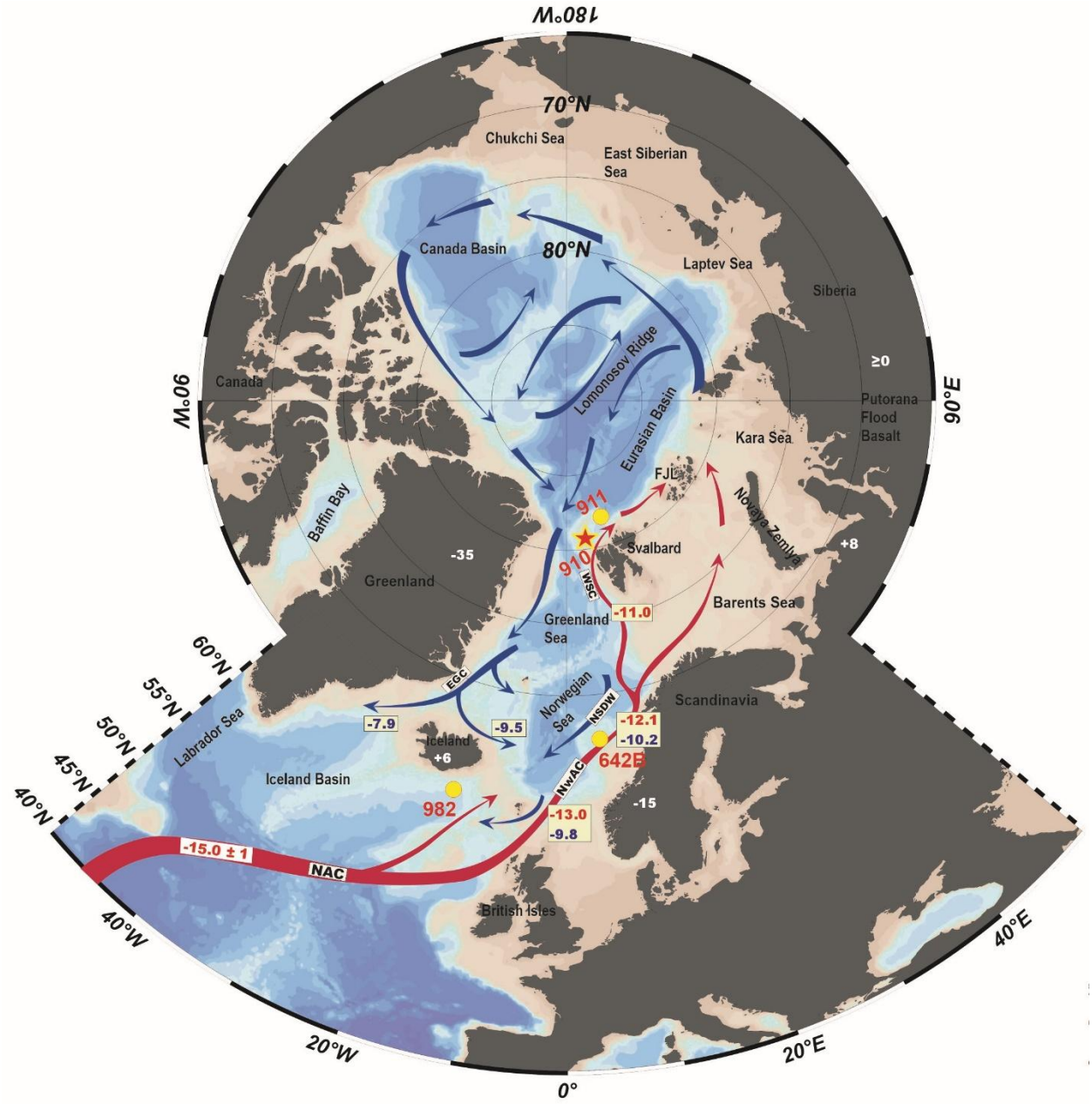

Fig. 1. Water mass circulation and their characteristic Nd isotope compositions. Locations of ODP Sites 910 (red star) and 911 (filled yellow circle) with schematic flow paths of the main water masses in the northern North Atlantic and Nordic Seas and their present-day ε_{Nd} signatures(Teschner et al., 2016). Dark red arrows mark the warm inflowing Atlantic water; dark blue arrows represent the cold deep and surface water masses flowing out of the Arctic Ocean(Andersson et al., 2008; François and Catherine,

2004; Lacan and Jeandel, 2004). White numbers mark the average ε_{Nd} values of the bedrocks of Svalbard(Tütken et al., 2002), the Norwegian Caledonian Margin and Iceland(Laskar et al., 2004), the Putorana basalts in Russia (Sharma et al., 1992), and Greenland (François and Catherine, 2004). Positions of ODP site 982 (58° N, 16° W) and ODP Hole 642B (67° 20′ N, 2° 90′ E) are shown.

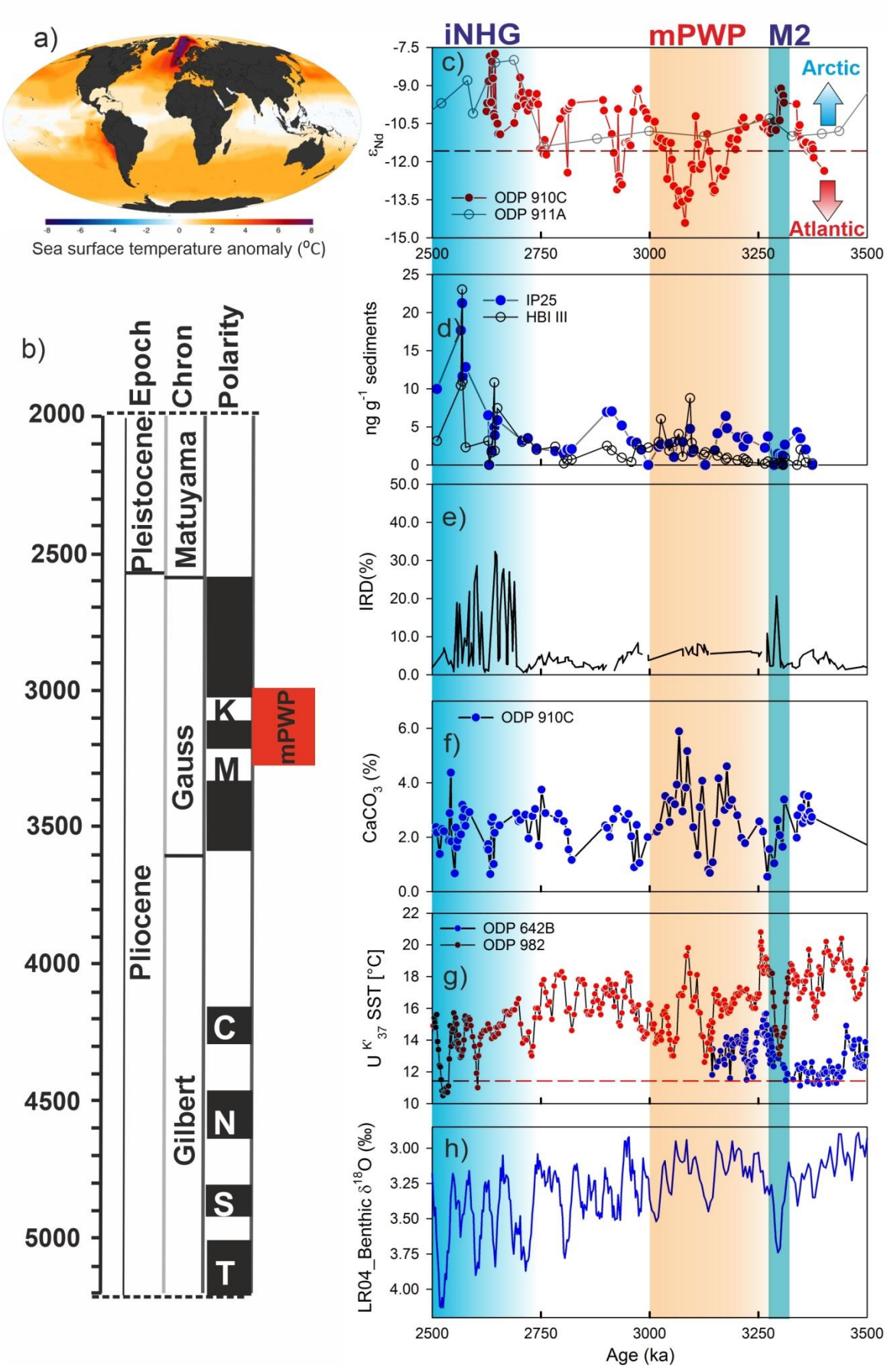

Fig. 2. Water mass exchange and associated changes in the Fram Strait during the Late-Pliocene and Pleistocene (a) Sea surface temperature (SST) anomalies during the mPWP (~3.3 – 3.0 Ma) compared to today (Dowsett et al., 2009). b) Pliocene-Pleistocene time scale with paleo-magnetic reversals. Red block represents the time slice of mPWP. c) Authigenic ε_{Nd} record from 910C (this study) and 911A (Teschner et al., 2016). d) Record of sea ice and open water biomarkers IP_{25} and HBI III. (e) Record of IRD (%) from ODP site 911A (Knies et al., 2014b). f) Record of $CaCO_3$ abundance (wt. %). g) Record of alkenon UK_{37} derived SST at ODP Sites 982(Lawrence et al., 2009) (58° N, 16° W) and ODP Hole 642B(Bachem et al., 2017) (67° 20′ N, 2° 90′ E). Dashed lines indicate Holocene average SSTs for the Norwegian Sea(Calvo et al., 2002) at 11.6 °C. h) Benthic $\delta^{18}O$ (LR04) stack(Lisiecki and Raymo, 2005). The shaded bands represent the major climatic transitions: M2 glaciation (blue shade, 3.312–3.264 Ma), mid-Pliocene Warm Period (mPWP) (brown shade, 3.3–3.0 Ma) and intensification Northern Hemisphere glaciation (iNHG, ~2.7 Ma).

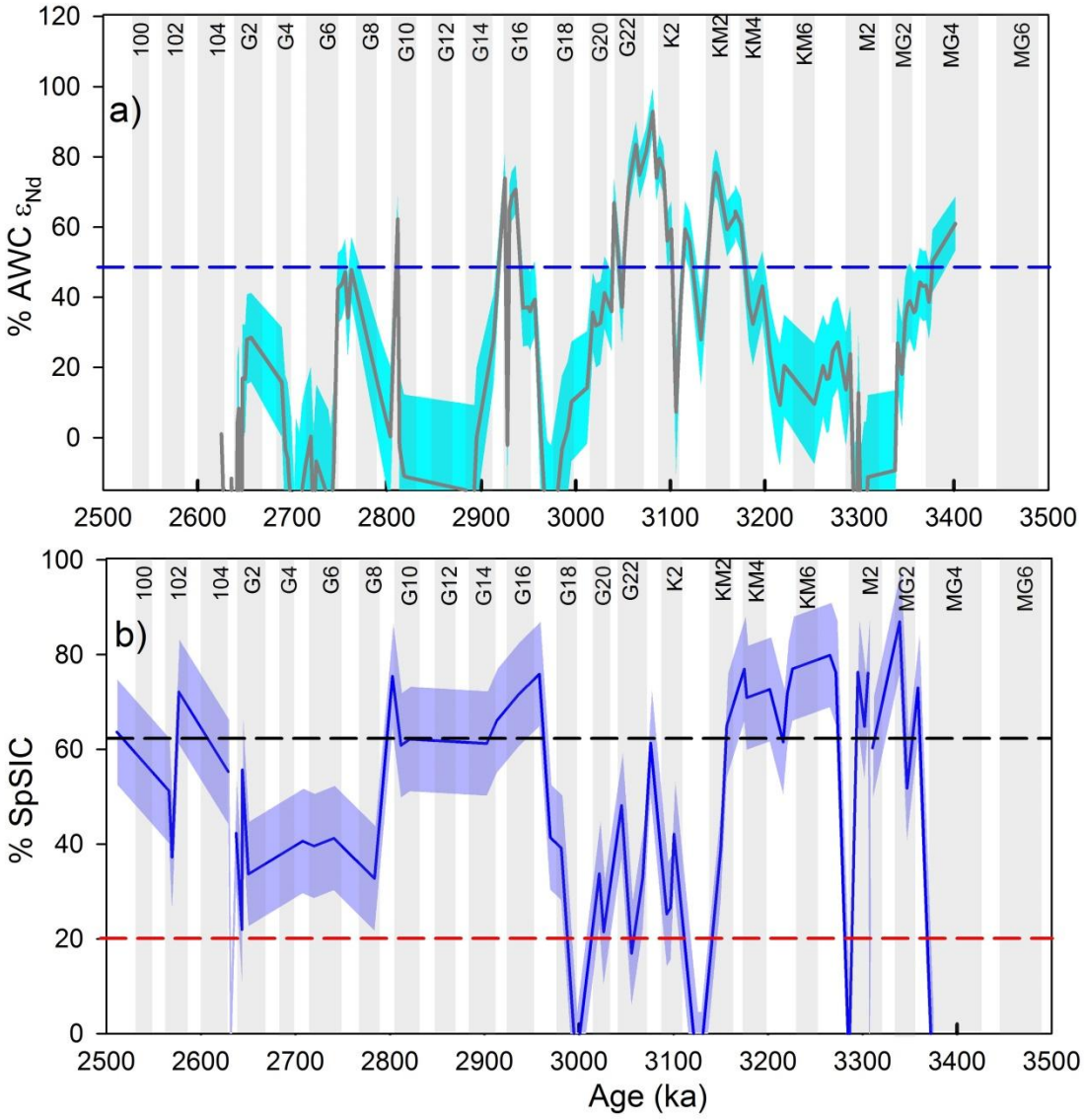

Fig. 3. North Atlantic (NAC) volume transport and corresponding Arctic Sea Ice changes. a) Fraction of Atlantic Water Component (%AWCε_{Nd}). Dark gray line: Best estimate. Shading: 95% confidence interval. Blue dashed line indicates modern Atlantic flow based on mooring estimate (Beszczynska-Moeller et al., 2012). (b) Spring sea ice (%). Solid blue line represents mean value. Blue shade represents root-mean-square error (RMSE) on the mean value. Blue and red dashed horizontal lines represent the modern mean (1988-2017, NSIDC) sea ice maximum (62%, Apr-June; spring) and minimum (20%, September; late summer) concentrations at the core site.

630

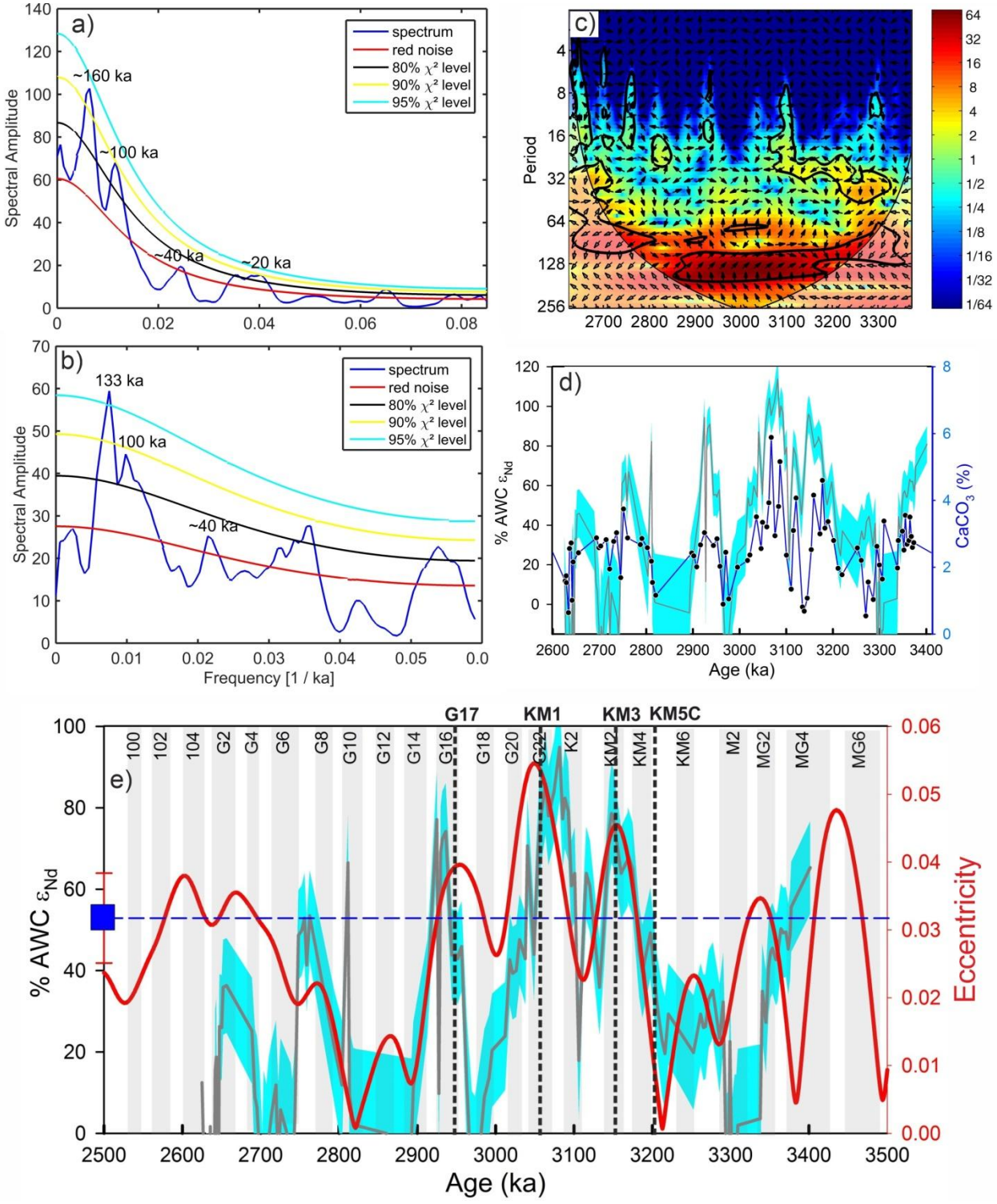

631

632 **Fig. 4. Identification of orbital cycles in proxy records**. Power spectrum analysis of (a) NAC volume

633 transport and (b) $CaCO_3$ abundance (%) records from the Yermak Plateau. They show periodicities of

orbital cycles at different significance level. c) Cross wavelet analysis of two time series highlights the common highest power between these two time series which is highlighted in color code. Vector arrow indicates phase relation between the time series. The 5% significance level against red noise is shown as a thick contour. The thin solid line indicates cone of influence. The relative phase relationship is shown as arrows (with in-phase pointing right, anti-phase pointing left, and ε_{Nd} leading $CaCO_3$ by 90° pointing straight down and vice versa). d) Comparison of the record of NAC with $CaCO_3$ percentage, an indicator of marine productivity. Both the curves overall follow the same pattern; the highest abundance in calcium carbonate and thus the highest productivity was observed during mPWP when NAC flow was maximum.

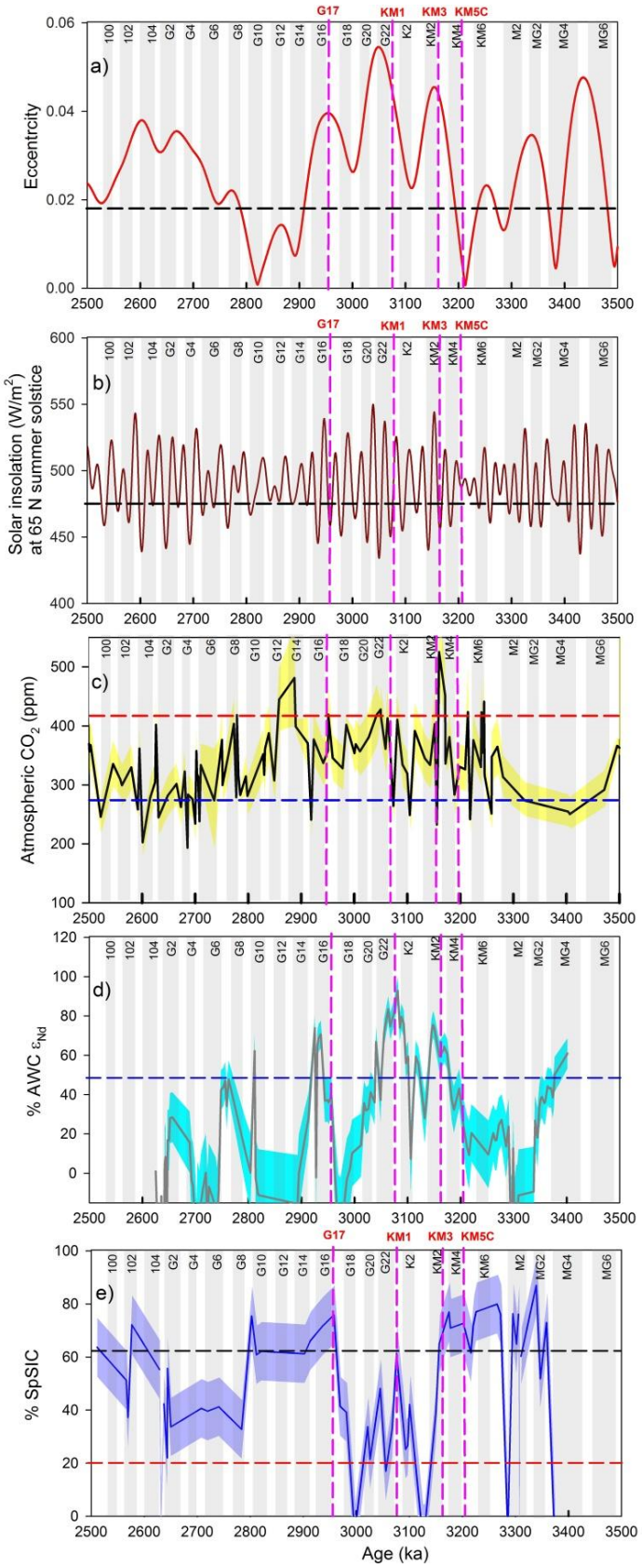

642

643 **Fig. 5 Role of orbital forcing in modulating watermass exchange and spring sea ice extent.** (a)
644 Record of eccentricity (Laskar et al., 2004). Dashed horizontal line represents modern eccentricity.
645 Vertical dashed lines (pink) indicate four interglacial periods KM5C, KM3, KM1 and G17. Among these
646 four interglacial periods, KM5C is most similar to that of the modern orbital forcing(Haywood and Valdes,
647 2004). (b) Record of solar insolation at 60° N summer solstice (Laskar et al., 2004). Dashed line
648 represents modern value of summer insolation. c) Record of atmospheric pCO_2 derived from boron
649 isotopes ($\delta^{11}B$) (Foster et al., 2017). Yellow band represents error envelops (1σ SD). Black and red colour
650 dashed lines represent pre-industrial CO_2 (280 ppm) and present CO_2 (~410 ppm) level. These forcing
651 parameters are compared with fraction of d) Atlantic Water (%AWC) and (e) Spring sea ice (%).

652

653

654

655

656

657

658

659

660

661

662

663

References

Andersson, P.S., Porcelli, D., Frank, M., Björk, G., Dahlqvist, R., Gustafsson, Ö., 2008. Neodymium isotopes in seawater from the Barents Sea and Fram Strait Arctic–Atlantic gateways. Geochimica et Cosmochimica Acta 72, 2854-2867.

Bachem, P.E., Risebrobakken, B., De Schepper, S., McClymont, E.L., 2017. Highly variable Pliocene sea surface conditions in the Norwegian Sea. Clim. Past 13, 1153-1168.

Bailey, I., Hole, G.M., Foster, G.L., Wilson, P.A., Storey, C.D., Trueman, C.N., Raymo, M.E., 2013. An alternative suggestion for the Pliocene onset of major northern hemisphere glaciation based on the geochemical provenance of North Atlantic Ocean ice-rafted debris. Quaternary Science Reviews 75, 181-194.

Ballantyne, A.P., Axford, Y., Miller, G.H., Otto-Bliesner, B.L., Rosenbloom, N., White, J.W.C., 2013. The amplification of Arctic terrestrial surface temperatures by reduced sea-ice extent during the Pliocene. Palaeogeography, Palaeoclimatology, Palaeoecology 386, 59-67.

Belt, S.T., 2018. Source-specific biomarkers as proxies for Arctic and Antarctic sea ice. Organic Geochemistry 125, 277-298.

Belt, S.T., Brown, T.A., Rodriguez, A.N., Sanz, P.C., Tonkin, A., Ingle, R., 2012. A reproducible method for the extraction, identification and quantification of the Arctic sea ice proxy IP25 from marine sediments. Analytical Methods 4, 705-713.

Belt, S.T., Cabedo-Sanz, P., Smik, L., Navarro-Rodriguez, A., Berben, S.M.P., Knies, J., Husum, K., 2015. Identification of paleo Arctic winter sea ice limits and the

687 marginal ice zone: Optimised biomarker-based reconstructions of late
688 Quaternary Arctic sea ice. Earth and Planetary Science Letters 431, 127-139.
689 Berends, C.J., de Boer, B., Dolan, A.M., Hill, D.J., van de Wal, R.S.W., 2019. Modelling
690 ice sheet evolution and atmospheric CO2 during the Late Pliocene. Clim. Past
691 15, 1603-1619.
692 Beszczynska-Moeller, A., Fahrbach, E., Schauer, U., Hansen, E., 2012. Variability in
693 Atlantic water temperature and transport at the entrance to the Arctic Ocean,
694 1997-2010.
695 Blake-Mizen, K., Hatfield, R.G., Stoner, J.S., Carlson, A.E., Xuan, C., Walczak, M.,
696 Lawrence, K.T., Channell, J.E.T., Bailey, I., 2019. Southern Greenland glaciation
697 and Western Boundary Undercurrent evolution recorded on Eirik Drift during the
698 late Pliocene intensification of Northern Hemisphere glaciation. Quaternary
699 Science Reviews 209, 40-51.
700 Cabedo-Sanz, P., Belt, S.T., 2016. Seasonal sea ice variability in eastern Fram Strait
701 over the last 2000 years. arktos 2, 22.
702 Calvo, E., Grimalt, J., Jansen, E., 2002. High resolution U37K sea surface temperature
703 reconstruction in the Norwegian Sea during the Holocene. Quaternary Science
704 Reviews 21, 1385-1394.
705 Chen, T.-Y., Frank, M., Haley, B.A., Gutjahr, M., Spielhagen, R.F., 2012. Variations of
706 North Atlantic inflow to the central Arctic Ocean over the last 14 million years
707 inferred from hafnium and neodymium isotopes. Earth and Planetary Science
708 Letters 353-354, 82-92.

709 Chow, N., Morad, S., Al-Aasm, I., 1996. Origin of Authigenic Carbonates in Eocene to
710 Quaternary Sediments from the Arctic Ocean and Norwegian-Greenland Sea.
711 Proceedings of the Ocean Drilling Program, Scientific Results 151.
712 Clotten, C., Stein, R., Fahl, K., De Schepper, S., 2018. Seasonal sea ice cover during
713 the warm Pliocene: Evidence from the Iceland Sea (ODP Site 907). Earth and
714 Planetary Science Letters 481, 61-72.
715 De Schepper, S., Schreck, M., Beck, K.M., Matthiessen, J., Fahl, K., Mangerud, G.,
716 2015. Early Pliocene onset of modern Nordic Seas circulation related to ocean
717 gateway changes. Nature Communications 6, 8659.
718 Ding, Q., Schweiger, A., L’Heureux, M., Steig, E.J., Battisti, D.S., Johnson, N.C.,
719 Blanchard-Wrigglesworth, E., Po-Chedley, S., Zhang, Q., Harnos, K., Bushuk,
720 M., Markle, B., Baxter, I., 2018. Fingerprints of internal drivers of Arctic sea ice
721 loss in observations and model simulations. Nature Geoscience.
722 Dowsett, H., Robinson, M., Haywood, A.M., Salzmann, U., Hill, D., Sohl, L.E., Chandler,
723 M., Williams, M., Foley, K., Stoll, D.K., 2010. The PRISM3D paleoenvironmental
724 reconstruction. Stratigraphy 7, 123-139.
725 Dowsett, H.J., Cronin, T.M., Poore, R.Z., Thompson, R.S., Whatley, R.C., Wood, A.M.,
726 1992. Micropaleontological Evidence for Increased Meridional Heat Transport in
727 the North Atlantic Ocean During the Pliocene. Science 258, 1133-1135.
728 Dowsett, H.J., Robinson, M.M., Foley, K.M., 2009. Pliocene three-dimensional global
729 ocean temperature reconstruction. Clim. Past 5, 769-783.
730 Dowsett, H.J., Robinson, M.M., Haywood, A.M., Hill, D.J., Dolan, A.M., Stoll, D.K.,
731 Chan, W.-L., Abe-Ouchi, A., Chandler, M.A., Rosenbloom, N.A., Otto-Bliesner,

B.L., Bragg, F.J., Lunt, D.J., Foley, K.M., Riesselman, C.R., 2012. Assessing confidence in Pliocene sea surface temperatures to evaluate predictive models. Nature Climate Change 2, 365.

Dubois-Dauphin, Q., Colin, C., Bonneau, L., Montagna, P., Wu, Q., Van Rooij, D., Reverdin, G., Douville, E., Thil, F., Waldner, A., Frank, N., 2017. Fingerprinting Northeast Atlantic water masses using neodymium isotopes. Geochimica et Cosmochimica Acta 210, 267-288.

Foster, G.L., Royer, D.L., Lunt, D.J., 2017. Future climate forcing potentially without precedent in the last 420 million years. Nature Communications 8, 14845.

François, L., Catherine, J., 2004. Neodymium isotopic composition and rare earth element concentrations in the deep and intermediate Nordic Seas: Constraints on the Iceland Scotland Overflow Water signature. Geochemistry, Geophysics, Geosystems 5.

Frank, M., 2002. RADIOGENIC ISOTOPES: TRACERS OF PAST OCEAN CIRCULATION AND EROSIONAL INPUT. Reviews of Geophysics 40, 1-1-1-38.

Grøsfjeld, K., De Schepper, S., Fabian, K., Husum, K., Baranwal, S., Andreassen, K., Knies, J., 2014. Dating and palaeoenvironmental reconstruction of the sediments around the Miocene/Pliocene boundary in Yermak Plateau ODP Hole 911A using marine palynology. Palaeogeography, Palaeoclimatology, Palaeoecology 414, 382-402.

Haley, B.A., Frank, M., Spielhagen, R.F., Eisenhauer, A., 2007. Influence of brine formation on Arctic Ocean circulation over the past 15 million years. Nature Geoscience 1, 68.

755 Haywood, A.M., Dowsett, H.J., Dolan, A.M., 2016. Integrating geological archives and
756 climate models for the mid-Pliocene warm period. Nature Communications 7,
757 10646.
758 Haywood, A.M., Hill, D.J., Dolan, A.M., Otto-Bliesner, B.L., Bragg, F., Chan, W.L.,
759 Chandler, M.A., Contoux, C., Dowsett, H.J., Jost, A., Kamae, Y., Lohmann, G.,
760 Lunt, D.J., Abe-Ouchi, A., Pickering, S.J., Ramstein, G., Rosenbloom, N.A.,
761 Salzmann, U., Sohl, L., Stepanek, C., Ueda, H., Yan, Q., Zhang, Z., 2013.
762 Large-scale features of Pliocene climate: results from the Pliocene Model
763 Intercomparison Project. Clim. Past 9, 191-209.
764 Haywood, A.M., Valdes, P.J., 2004. Modelling Pliocene warmth: contribution of
765 atmosphere, oceans and cryosphere. Earth and Planetary Science Letters 218,
766 363-377.
767 Horikawa, K., Martin, E.E., Basak, C., Onodera, J., Seki, O., Sakamoto, T., Ikehara, M.,
768 Sakai, S., Kawamura, K., 2015. Pliocene cooling enhanced by flow of low-
769 salinity Bering Sea water to the Arctic Ocean. Nature Communications 6, 7587.
770 Huber, R., Meggers, H., Baumann, K.H., Henrich, R., 2000. Recent and Pleistocene
771 carbonate dissolution in sediments of the Norwegian–Greenland Sea. Marine
772 Geology 165, 123-136.
773 IPCC, 2013. Climate Change 2013: The Physical Science Basis. Contribution of
774 Working Group I to the Fifth Assessment Report of the Intergovernmental Panel
775 on Climate Change. Cambridge University Press, Cambridge, United Kingdom
776 and New York, NY, USA.

777 Kinnard, C., Zdanowicz, C.M., Fisher, D.A., Isaksson, E., de Vernal, A., Thompson,
778 L.G., 2011. Reconstructed changes in Arctic sea ice over the past 1,450 years.
779 Nature 479, 509.
780 Knies, J., Cabedo-Sanz, P., Belt, S.T., Baranwal, S., Fietz, S., Rosell-Melé, A., 2014a.
781 The emergence of modern sea ice cover in the Arctic Ocean. Nature
782 Communications 5, 5608.
783 Knies, J., Matthiessen, J., Vogt, C., Stein, R., 2002. Evidence of ‘Mid-Pliocene (˜3 Ma)
784 global warmth’ in the eastern Arctic Ocean and implications for the
785 Svalbard/Barents Sea ice sheet during the late Pliocene and early Pleistocene
786 (˜3 – 1.7 Ma). Boreas 31, 82-93.
787 Knies, J., Mattingsdal, R., Fabian, K., Grøsfjeld, K., Baranwal, S., Husum, K., De
788 Schepper, S., Vogt, C., Andersen, N., Matthiessen, J., Andreassen, K., Jokat,
789 W., Nam, S.-I., Gaina, C., 2014b. Effect of early Pliocene uplift on late Pliocene
790 cooling in the Arctic–Atlantic gateway. Earth and Planetary Science Letters 387,
791 132-144.
792 Köseoğlu, D., Belt, S.T., Husum, K., Knies, J., 2018. An assessment of biomarker-
793 based multivariate classification methods versus the PIP25 index for paleo Arctic
794 sea ice reconstruction. Organic Geochemistry 125, 82-94.
795 Lacan, F., Jeandel, C., 2004. Denmark Strait water circulation traced by heterogeneity
796 in neodymium isotopic compositions. Deep Sea Research Part I: Oceanographic
797 Research Papers 51, 71-82.
798 Lambelet, M., van de Flierdt, T., Crocket, K., Rehkämper, M., Kreissig, K., Coles, B.,
799 Rijkenberg, M.J.A., Gerringa, L.J.A., de Baar, H.J.W., Steinfeldt, R., 2016.

Neodymium isotopic composition and concentration in the western North Atlantic Ocean: Results from the GEOTRACES GA02 section. Geochimica et Cosmochimica Acta 177, 1-29.

Lang, D.C., Bailey, I., Wilson, P.A., Chalk, T.B., Foster, G.L., Gutjahr, M., 2016. Incursions of southern-sourced water into the deep North Atlantic during late Pliocene glacial intensification. Nature Geoscience 9, 375.

Laskar, J., Robutel, P., Joutel, F., Gastineau, M., Correia, A.C.M., Levrard, B., 2004. A long-term numerical solution for the insolation quantities of the Earth. A&A 428, 261-285.

Laukert, G., Frank, M., Bauch, D., Hathorne, E.C., Rabe, B., von Appen, W.-J., Wegner, C., Zieringer, M., Kassens, H., 2017. Ocean circulation and freshwater pathways in the Arctic Mediterranean based on a combined Nd isotope, REE and oxygen isotope section across Fram Strait. Geochimica et Cosmochimica Acta 202, 285-309.

Lawrence, K., Herbert, T., M. Brown, C., Raymo, M., M. Haywood, A., 2009. High amplitude variations in North Atlantic sea surface temperature during the Early Pliocene Warm Period.

Lisiecki, L.E., Raymo, M.E., 2005. A Pliocene-Pleistocene stack of 57 globally distributed benthic δ18O records. Paleoceanography 20.

Martin, F., 2002. RADIOGENIC ISOTOPES: TRACERS OF PAST OCEAN CIRCULATION AND EROSIONAL INPUT. Reviews of Geophysics 40, 1-1-1-38.

821 Mattingsdal, R., Knies, J., Andreassen, K., Fabian, K., Husum, K., Grøsfjeld, K., De
822 Schepper, S., 2014. A new 6 Myr stratigraphic framework for the Atlantic–Arctic
823 Gateway. Quaternary Science Reviews 92, 170-178.
824 Müller, J., Wagner, A., Fahl, K., Stein, R., Prange, M., Lohmann, G., 2011. Towards
825 quantitative sea ice reconstructions in the northern North Atlantic: A combined
826 biomarker and numerical modelling approach. Earth and Planetary Science
827 Letters 306, 137-148.
828 Müller, J., Werner, K., Stein, R., Fahl, K., Moros, M., Jansen, E., 2012. Holocene
829 cooling culminates in sea ice oscillations in Fram Strait. Quaternary Science
830 Reviews 47, 1-14.
831 Naafs, B.D.A., Stein, R., Hefter, J., Khélifi, N., De Schepper, S., Haug, G.H., 2010. Late
832 Pliocene changes in the North Atlantic Current. Earth and Planetary Science
833 Letters 298, 434-442.
834 Petrie, R.E., Shaffrey, L.C., Sutton, R.T., 2015. Atmospheric Impact of Arctic Sea Ice
835 Loss in a Coupled Ocean–Atmosphere Simulation. Journal of Climate 28, 9606-
836 9622.
837 Polyakov, I.V., Pnyushkov, A.V., Alkire, M.B., Ashik, I.M., Baumann, T.M., Carmack,
838 E.C., Goszczko, I., Guthrie, J., Ivanov, V.V., Kanzow, T., Krishfield, R., Kwok,
839 R., Sundfjord, A., Morison, J., Rember, R., Yulin, A., 2017. Greater role for
840 Atlantic inflows on sea-ice loss in the Eurasian Basin of the Arctic Ocean.
841 Science 356, 285-291.

Prescott, C.L., Dolan, A.M., Haywood, A.M., Hunter, S.J., Tindall, J.C., 2018. Regional climate and vegetation response to orbital forcing within the mid-Pliocene Warm Period: A study using HadCM3. Global and Planetary Change 161, 231-243.

R Core Team, 2018. R: A language and environment for statistical computing. R Foundation for Statistical Computing. Vienna, Austria URL http://www.R-project.org/.

Raymo, M.E., Grant, B., Horowitz, M., Rau, G.H., 1996. Mid-Pliocene warmth: stronger greenhouse and stronger conveyor. Marine Micropaleontology 27, 313-326.

Rempfer, J., Stocker, T.F., Joos, F., Dutay, J.-C., Siddall, M., 2011. Modelling Nd-isotopes with a coarse resolution ocean circulation model: Sensitivities to model parameters and source/sink distributions. Geochimica et Cosmochimica Acta 75, 5927-5950.

Sato, T., Kameo, K., 1996. Pliocene to Quaternary calcareous nannofossil biostratig-raphy of the Arctic Ocean, with reference to late Pliocene glaciation. W.F. (Eds.), Proc. ODP, Sci. Results 151.

Sharma, M., Basu, A.R., Nesterenko, G.V., 1992. Temporal Sr-, Nd- and Pb-isotopic variations in the Siberian flood basalts: Implications for the plume-source characteristics. Earth and Planetary Science Letters 113, 365-381.

Smik, L., Cabedo-Sanz, P., Belt, S.T., 2016. Semi-quantitative estimates of paleo Arctic sea ice concentration based on source-specific highly branched isoprenoid alkenes: A further development of the PIP25 index. Organic Geochemistry 92, 63-69.

Spielhagen, R.F., Werner, K., Sørensen, S.A., Zamelczyk, K., Kandiano, E., Budeus, G., Husum, K., Marchitto, T.M., Hald, M., 2011. Enhanced Modern Heat Transfer to the Arctic by Warm Atlantic Water. Science 331, 450-453.

Stein, R., Fahl, K., Gierz, P., Niessen, F., Lohmann, G., 2017. Arctic Ocean sea ice cover during the penultimate glacial and the last interglacial. Nature Communications 8, 373.

Tachikawa, K., Jeandel, C., Roy-Barman, M., 1999. A new approach to the Nd residence time in the ocean: the role of atmospheric inputs. Earth and Planetary Science Letters 170, 433-446.

Tanaka, T., Togashi, S., Kamioka, H., Amakawa, H., Kagami, H., Hamamoto, T., Yuhara, M., Orihashi, Y., Yoneda, S., Shimizu, H., Kunimaru, T., Takahashi, K., Yanagi, T., Nakano, T., Fujimaki, H., Shinjo, R., Asahara, Y., Tanimizu, M., Dragusanu, C., 2000. JNdi-1: A neodymium isotopic reference in consistency with LaJolla neodymium.

Teschner, C., Frank, M., Haley, B.A., Knies, J., 2016. Plio-Pleistocene evolution of water mass exchange and erosional input at the Atlantic-Arctic gateway. Paleoceanography 31, 582-599.

Tütken, T., Eisenhauer, A., Wiegand, B., Hansen, B.T., 2002. Glacial–interglacial cycles in Sr and Nd isotopic composition of Arctic marine sediments triggered by the Svalbard/Barents Sea ice sheet. Marine Geology 182, 351-372.

Vogt, C., Knies, J., Spielhagen, R.F., Stein, R., 2001. Detailed mineralogical evidence for two nearly identical glacial/deglacial cycles and Atlantic water advection to

the Arctic Ocean during the last 90,000 years. Global and Planetary Change 31, 23-44.

Werner, K., Frank, M., Teschner, C., Müller, J., F. Spielhagen, R., 2014. Neoglacial change in deep water exchange and increase of sea-ice transport through eastern Fram Strait: Evidence from radiogenic isotopes.

Zamelczyk, K., Rasmussen, T.L., Husum, K., Godtliebsen, F., Hald, M., 2014. Surface water conditions and calcium carbonate preservation in the Fram Strait during marine isotope stage 2, 28.8–15.4 kyr. Paleoceanography 29, 1-12.

Zhang, Z.S., Nisancioglu, K.H., Chandler, M.A., Haywood, A.M., Otto-Bliesner, B.L., Ramstein, G., Stepanek, C., Abe-Ouchi, A., Chan, W.L., Bragg, F.J., Contoux, C., Dolan, A.M., Hill, D.J., Jost, A., Kamae, Y., Lohmann, G., Lunt, D.J., Rosenbloom, N.A., Sohl, L.E., Ueda, H., 2013. Mid-pliocene Atlantic Meridional Overturning Circulation not unlike modern. Clim. Past 9, 1495-1504.